Carbon 182 (2021) 799–805

Contents lists available at ScienceDirect

Carbon

journal homepage: www.elsevier.com/locate/carbon

Ascorbic acid-assisted defect healing and stack ordering of graphene films towards high power thermal dispersion

Zuo Pan [a, b], Yanhong Wu [c], Hong Yuan [a, e], Runli Tang [c], Lei Ji [c], Bucun Zhou [d], Chuanren Ye [a, e], Dawei Zhang [f], Yan Qu [c], Hengxing Ji [a, e, **], Yanwu Zhu [a, e, *]

[a] Institute of Advanced Technology, University of Science and Technology of China, Hefei, 230026, China
[b] Shenzhen Qianhai Ruiji Technology Co., Ltd., Shenzhen, 518000, China
[c] The Sixth Element (Changzhou) Materials Technology Co., Ltd., Changzhou, 213000, China
[d] Changzhou Fuxi Technology Co., Ltd., Changzhou, 213000, China
[e] Hefei National Research Center for Physical Sciences at the Microscale, CAS Key Laboratory of Materials for Energy Conversion, School of Chemistry and Materials Science, University of Science and Technology of China, Hefei, 230026, China
[f] School of Chemical Engineering, Hefei University of Technology, Hefei, 230026, China

ARTICLE INFO

Article history:
Received 20 February 2021
Received in revised form
10 June 2021
Accepted 16 June 2021
Available online 30 June 2021

Keywords:
Ascorbic acid
Defect healing
Thick graphene films
Thermal dispersion

ABSTRACT

The thermal dispersion power depends on thermal conductivity and thickness of the thermal dispersion material that is a critical component of modern electronic devices due to the demands of high operating power in a miniaturized space. Films made of assembled graphene flakes have been becoming an emerging thermal dispersion material owing to their high thermal conductivity and tunable thickness up to millimeters, which outperform that of artificial graphite films made from polyimide. But the thermal conductivity typically decreases with the increase of film thickness. In our work, by pre-reducing the graphene oxide with Vitamin C and sequentially annealing the stacking films at 2950 °C, a 80 μm-thick graphene film (GF) with an in-plane thermal conductivity of above 1600 W/(m·K) is achieved. Detailed characterizations indicate that, the addition of Vitamin C is beneficial to the assembly ordering of graphene oxide platelets and the defect healing during the thermal annealing, which both contribute to the excellent thermal conductivity of the films. Our work provides an industrially scalable strategy towards high performance heat dissipation films for future electronic devices.

1. Introduction

In the rapid development of communication power and the miniaturization of electronic equipment, enormous amount of heat is generated, especially in the high-frequency and high-speed transmission. Thus, thermal management materials with ability of instantaneous heat dissipation are critical to the operation reliability and performance stability of the electronic devices. Currently, the high-performance thermal dissipation films used in commercial electronic devices are mostly fabricated by carbonization and graphitization of polyimide (PI) films, possessing a typical in-plane thermal conductivity in the range of 1200–1500 W/(m·K) [1–3]. Limited by the production technique of highly oriented PI films, however, the PI derived graphite films generally have limited range of thicknesses; it is challenging to achieve such films with a thickness larger than 30 μm [4]. In contrast, many electronic devices, *e.g.*, 5G communicating devices operating at high power, require heat dissipation films simultaneously with a thickness larger than 80 μm and a thermal conductivity higher than 1500 W/(m·K).

On the other hand, the in-plane thermal conductivity of suspended graphene has been to be up to 5300 W/(m·K) near the room temperature [5]. More importantly, graphene films (donated as GFs) can be obtained by orderly stacking graphene oxide (GO) platelets and subsequent reduction/graphitization. The thickness of films derived from GO is highly tunable, *e.g.*, by controlling the coating thickness of GO suspension in the film preparation. The pioneering work on the stacking of GO platelets has been demonstrated by Ruoff's group [6]. Recently, the same group showed a thermal conductivity of up to 2025 ± 25 W/(m·K) from highly

* Corresponding author. Institute of Advanced Technology, University of Science and Technology of China, Hefei, 230026, China.
** Corresponding author. Institute of Advanced Technology, University of Science and Technology of China, Hefei, 230026, China.
E-mail addresses: jihengx@ustc.edu.cn (H. Ji), zhuyanwu@ustc.edu.cn (Y. Zhu).

https://doi.org/10.1016/j.carbon.2021.06.058
0008-6223/

densified 5 μm-thick GFs by mixing GO with reduced GO (rGO) flakes and annealing at 3000 °C [7]. Gao' s group also demonstrated a 10 μm-thick GFs with a thermal conductivity of 1940 ± 113 W/(m·K) [8]. Chen's group synthesized a graphitized GO/PI hybrid GFs with an in-plane thermal conductivity of 1428 ± 64 W/(m·K) for 30 μm thickness [9]. These works have demonstrated the great potential of GFs for high-performance thermal dissipation in electronic devices, but it is challenging to maintain an impressive in-plane thermal conductivity for thick films (*e.g.*, >80 μm). In particular, the compact-stacking layers in thick GO films would largely hamper the escape of gaseous species in graphene lamellae, which thus would be accumulated inside the films during the reduction and graphitization, consequently deforming the graphene platelets and leading to a deteriorated stacking order [8,10]. For example, the in-plane thermal conductivity of GFs retained ~1103 W/(m·K) for the thickness of 80 μm [11].

Challenges also remain with conventional thermal reduction methods below 1100 °C due to generation of gaseous specious (CO_2, CO, H_2O, *etc.*) and topological defects in the carbon skeleton [12]. Subsequent high temperature graphitization is necessary to remove the residual functional groups and to heal the defects. Previous studies have shown that the in-plane thermal conductivity of GFs is dominated by the crystalline domains size [13,14], the defect content in the graphene platelets and the lateral boundary between platelets [15–17]. Although various methods have been proposed to restore the structure of graphene, *e.g.*, by ethanol [18] or iron (III) chloride hexahydrate ($FeCl_3$) [19] assistant thermal treatment, extra carbon source or metallic species would generate more gas species or deteriorate the ordering of GO stacking. As the orientation of GFs film heavily affects the thermal conductivity [20], further optimized defect healing protocols while not to destroy the assembly ordering of GO stacking are needed to improve the thermal conductivity for thick GFs.

Herein, ascorbic acid (vitamin C, VC) is used as a mild reductant compared to other reductants such as hydrazine hydrate and hydroiodic acid [21]. The stable suspensions are achieved by pre-reduction of GO with 8 wt% VC; the hybrid slurry named as GO-VC can be assembled into highly ordered films by blade coating. Only containing C, H, and O elements, VC helps to heal the defects while avoiding the introduction of impurity atoms, and benefit to maintain the crystalline domains in the final graphitized films. Using this strategy, the 80 μm-thick GFs (named as rGO-VC-*x* film) demonstrated a superior thermal conductivity of up to 1600 W/(m·K).

2. Experimental

2.1. Materials

The raw material was commercially available wet GO cake, with a stock number of SE2430W–N produced by The Sixth Element Materials Technology Co. Ltd. Vitamin C was purchased from Shanghai Zhanyun Chemical Co., Ltd. (AR, 99.7%) for laboratory-scale fabrication or from Shandong Tongsheng Food Ingredients Co., Ltd. (feed grade) for large-scale production.

2.2. Preparation procedures

The wet cake containing ~50 wt% water was exfoliated into a homogeneous suspension in more water by high-pressure homogenization processing (ATS, AH-PILOT 2018), to a concentration of 3.5 wt%. The 3.5 wt% GO suspension was vigorously stirred and slowly added with VC. Then the mixture dispersion was further exfoliated by passing it twice through the high-pressure homogenization processor under a pressure of 850 MPa, from which GO-VC-*x* suspensions were obtained. Bubbles were eliminated from the suspensions under the vacuum. After that the suspension was blade-casted on a PET substrate, and dried in a blast oven at 80 °C for 2 h, to obtain GO-VC-*x* films. Then the GO-VC-*x* films were thermally treated by a programmed oven to 2950 °C for 2 h to obtain rGO-VC-*x* films. rGO-VC-*x* films were finally compressed under 70 MPa for 12 h.

2.3. Characterizations

Raman spectroscopy was performed using a confocal Raman microscope (Renishaw, inVia Reflex) with a laser wavelength of 488 nm thermogravimetric analysis (TGA) measurements (Netzsch, STA 449 F5) were performed from 25 to 1000 °C at a heating rate of 10 °C/min in a nitrogen atmosphere. X-ray photoelectron spectroscopy (XPS) was performed with Thermo Fisher, ESCALAB 250 xi and the spectra were fitted and deconvoluted using XPSPEAK41 software. Fourier-transform infrared (FT-IR) spectra were recorded with an infrared spectrometer (Tianjin Gangdong FTIR-650) in a scan range from 500 to 4000 cm^{-1} under the attenuated total reflectance (ATR) mode. X-ray diffraction (XRD) patterns were acquired using an X-ray diffractometer (Rigaku) equipped with a Cu K α radiation source (λ = 0.154184 nm). The zeta potential data were acquired using a ZEN3700 Nano ZSE. The tapping mode atomic force microscopy (AFM) were carried out using a Dimension Edge AFM (Bruker).

Cross-sectional scanning electron microscopy (SEM) images were obtained on a Navo NanoSEM450 (FEI) field-emission electron microscope at an accelerating voltage of 10 kV. The in-plane thermal conductivity was measured using a laser flash method using a NanoFlash instrument (Netzsch LFA 467). Cross-plane thermal conductivity was tested by Interface material thermal resistance and thermal conduction system instrument (LW 9389 Longwin). The density was measured by a vacuum densitometer (Builder, TD-2200). The thickness of films was acquired with a thickness gauge (Mitutoyo). The heat capacities were measured using a Netzsch DSC 3500 at 50 °C.

3. Results and discussion

Fig. 1 shows the fabrication procedure and optical images of rGO-VC-*x* films. In brief, a wet graphite oxide cake made by modified Hummers' method [22] was diluted to GO suspension with a concentration of 3.5 wt% by mechanical stirring for 1 h at the room temperature. Then certain amount of VC was introduced into the GO aqueous suspension by stirring for another 2 h. The hybrid films were made by blade coating of the GO-VC stock; the GO-VC-*x* films, where *x* represents the mass ratio of VC to GO were obtained by drying the coating at 80 °C for 2 h. Due to the release of gas and thermal stress during the treatment, foamed like GFs (F-rGO-VC-8%) show a low density of ~0.32 g/cm^3 (Fig. S1a) after the sequential thermal treatment at 1000 and 2950 °C. Without introduction of VC, F-rGO-VC-0% has an even lower density of ~0.23 g/cm^3. As seen from Fig. S1b, the typical size of air pocket in F-rGO-VC-8%, is ~10 μm, while that in F-rGO-VC-0% is 15–30 μm. After a mechanical pressing at ~70 MPa, compact rGO-VC-*x* films with density of ~2.14 g/cm^3 were obtained, as shown in Fig. S1c. The thickness of rGO-VC-*x* films ranges from 78 to 83 μm, as listed in Table S1.

To determine the role of VC, GO dispersions with various VC contents were characterized. From Fig. S3 we can see that the color of GO dispersions evolves from dark yellow to black with increase in the VC, indicating that GO has been reduced in the presence of VC. Correspondingly, SEM images in Fig. 2a and b and S4 reveal that GO platelets remains flat without wrinkles or agglomeration for $x \leq 8\%$. However, when the VC mass ratio exceeds 8%, GO starts to

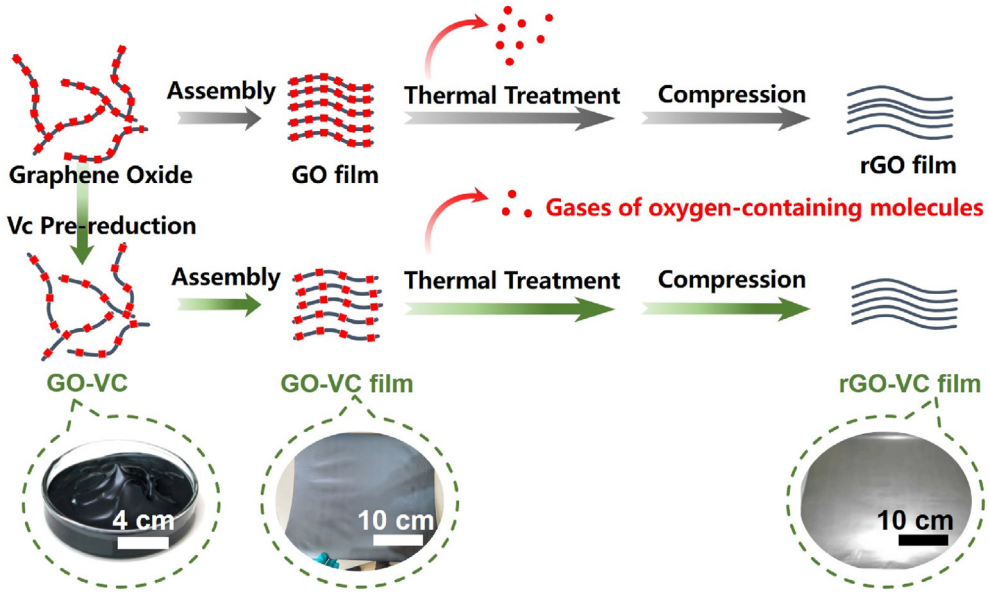

Fig. 1. Schematic of procedures to fabricate rGO-VC-*x* films. (A colour version of this figure can be viewed online.)

agglomerate or restack, as typically shown in the SEM image of GO-VC-20% in Fig. 2c. The AFM image in Fig. 2d has shown a thickness of ~0.78 nm measured across the platelets of GO-VC-8%. In comparison, the thickness of GO-VC-0%, GO-VC-5% or GO-VC-20% is ~0.8, ~0.75 or ~0.9 nm, respectively, as shown in Fig. S5. The slightly different thickness of GO platelets after introducing VC might be caused by removal of some functional groups [23]. Zeta potential testing was carried out to evaluate the stability of the GO-VC dispersions. As shown in Fig. 2e, the absolute value of zeta potential increases rapidly with introducing 1% VC, indicating the higher stability of GO-VC-1% than the bare GO suspension. The high zeta potential values maintain in the VC ratio ranging from 1% to 10%. When the amount of VC reaches 20%, however, the absolute value of zeta potential of GO-VC-20% decreases to that close to the bare GO suspension, which may explain the obvious agglomeration trend shown in the SEM above (Fig. 2c). Thus, the addition of proper amount of VC is beneficial to the stability of GO platelets in aqueous dispersions, which shall improve the assembly ordering during coating and drying.

The morphology of the blade coated GO-VC-*x* films was investigated to determine the effect of VC content on the assembly ordering of films. As shown in Fig. 3a–c and Fig. 3g–i, a smooth surface of GO-VC-*x* films is obtained for $x \leq 8\%$. However, cracks are observed in GO-VC-10% film (Fig. 3h) and the film even fragments into small pieces upon drying for GO-VC-20% (Fig. 3i). Correspondingly, the cross-sectional SEM images (Fig. 3d–f, 3j) demonstrate a layer-by-layer compact stacking morphology for $x \leq 8\%$. But the stacking structure becomes disordered when increasing the VC content to 10% (Fig. 3k). When the amount of VC reaches 20%, the cross-section of GO-VC-20% film (Fig. 3l) shows a heavy disordering with wrinkles and kinks. The assembly ordering of GO films is essentially related to the colloidal status of GO platelets, such as the dispersion and spreading of the platelets [24]. In the XRD pattern, GO-VC-0% shows a sharp peak and completely

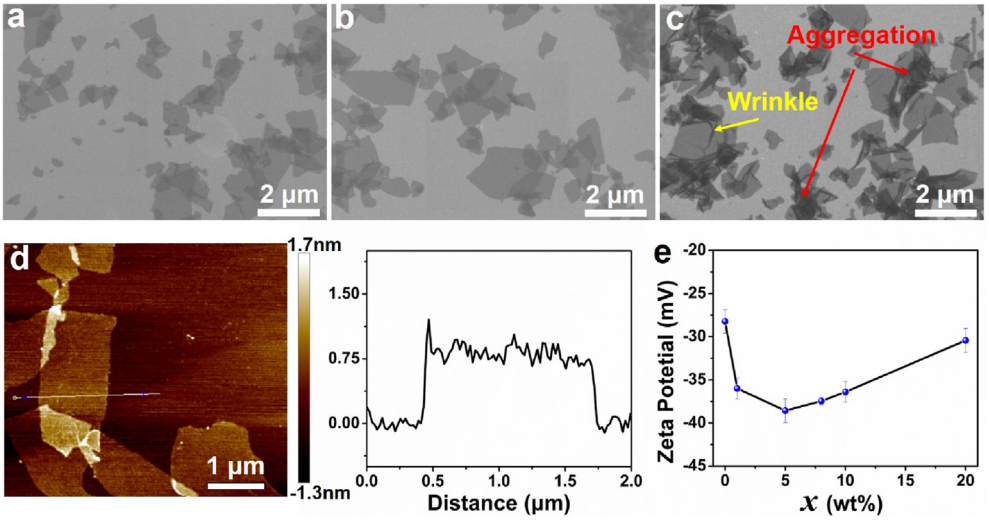

Fig. 2. SEM images of (a) GO-VC-0%, (b) GO-VC-8% and (c) GO-VC-20%. (d) AFM image and corresponding height profile of GO-VC-8%. (e) Zeta potential of GO-VC-*x* suspensions at 0.1 wt%. (A colour version of this figure can be viewed online.)

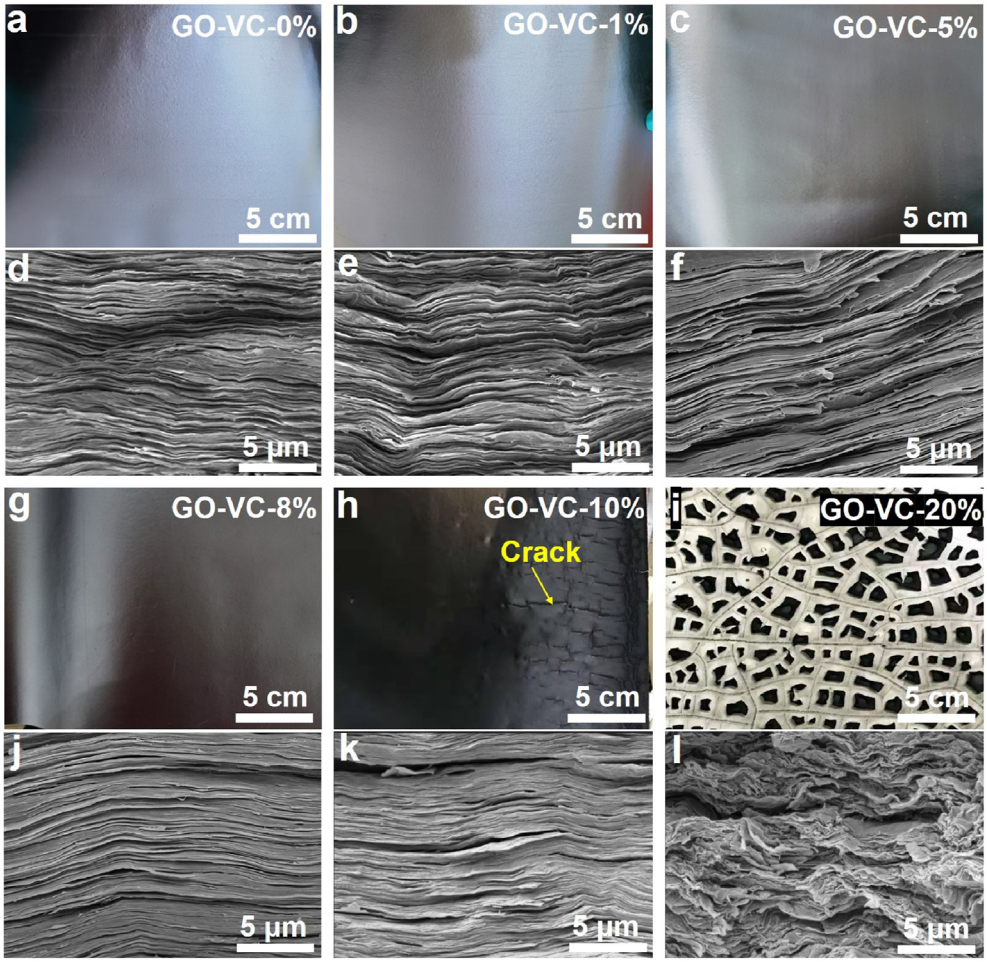

Fig. 3. Optical images (a-c, g-i) and cross-sectional SEM images (d-f, j-l) of GO-VC-*x* films. (A colour version of this figure can be viewed online.)

disappears when *x* increases up to 20% (Fig. S6a). The full width at half maximum (FWHM) corresponding to the interlayer peak for GO-VC-*x* films increases from 0.823° to 8.71° when *x* increases from 0 to 20% (Fig. S6b). Since FWHM is related to the distribution of the peak position, we presumably attribute the larger FWHM to the change in stack ordering of GO films, which is sensitive to the hydrophilic groups of GO. Combining all the characterizations, we can clearly see that a proper amount of VC (*e.g.*, ~8%) would promote the stability of GO suspensions while not disturbing the assembly ordering of GO films too much. Introducing more VC (*e.g.*, 10% or 20%) would cause the wrinkling or even sheets aggregation in the stacking, which eventually leads to the cracks or fragmentation of films upon drying.

The chemical feature of dried GO-VC-*x* films has been further characterized to clarify the effect of VC. As shown in the FT-IR spectra (Fig. 4a), the peaks at 1720, 1617, 1560, and 1370 cm^{-1} are ascribed to the stretching vibration of C═O, the bending vibration of H_2O, and the stretching vibrations of C═C and C—OH, respectively [25]. Several peaks of pure VC (Fig. S7) located at 3530, 3411, 3319, 1753, and 1663 cm^{-1}, have vanished in the spectra of GO-VC-*x* films, which means that VC reacted with the functional groups of GO. In addition, due to more hydrophobic feature of GO after certain degree of reduction by VC, the peak at ~1617 cm^{-1} (bending vibration of H_2O) gradually weakens as *x* increases, indicating less water absorption [25]. As a result, the peak intensities of 1560 cm^{-1} (C═C) and 1370 cm^{-1} (C—OH) enhances as *x* increases due to the pre-reduction with VC. Fig. 4b and Fig. S8a show the derivative thermo gravimetry (DTG) and TGA curves of GO-VC-*x* films, respectively. The obvious weight loss of bare GO and GO-VC-1% at ~100 °C (Fig. 4b) is due to the removal of water [26]. The less loss of water for GO-VC-*x* with larger *x* values is consistent to the FT-IR results, verifying the reduction in such films due to addition of VC. The temperature corresponding to the main weight loss evolves from ~227 °C for bare GO and GO-VC-1%, to lower temperature as *x* increases, till ~204 °C for GO-VC-10%. The other weigh loss at around 148 °C is significantly enhanced especially for *x* of 20%. Compared to the weight loss of pure VC between 194 °C and 253 °C, we can see that the introduction of VC has lowered the temperature needed for reduction, consistent with the FT-IR results [27]. The pre-reduction would be beneficial to the high temperature annealing as less gas species shall be generated in the following treatment.

Raman spectroscopy has been used to investigate the structural evolution by analyzing the changes in D-band and G-band [28,29]. As shown in Fig. 4c, the FWHM of D-band becomes smaller with addition of VC, indicating the lower content of defects in a graphitic lattice [28]. But the I_D/I_G ratio (Fig. S8c) does not change significantly, showing the relatively weak reduction [30,31]. XPS was further used to analyze the elemental composition of GO-VC-*x* films. The C/O atomic ratio is about 1.57, 2.48, and 2.15 for GO-VC-0%, GO-VC-8%, and GO-VC-20%, respectively (Fig. S8b), indicating the reduction for $x = 8\%$. But more VC adsorbed on GO sheet

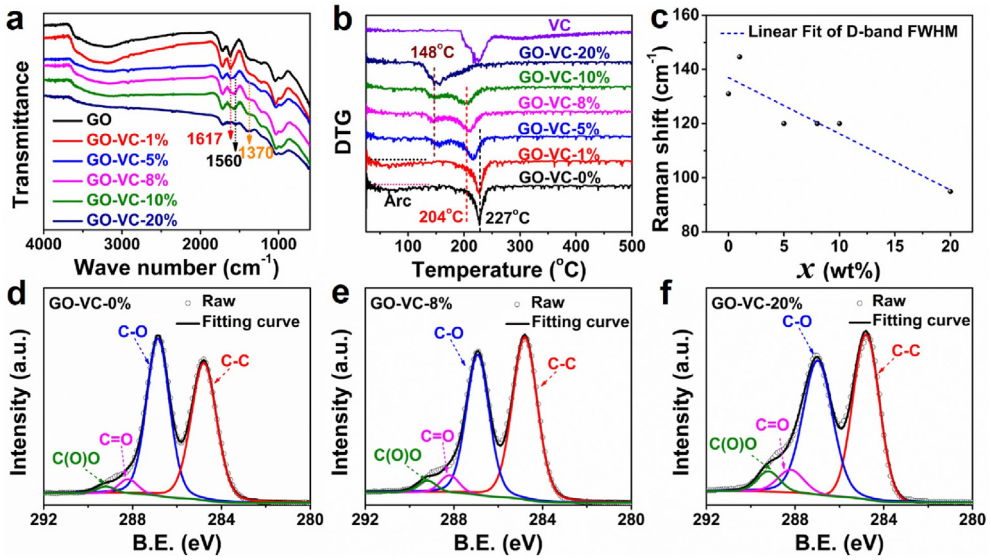

Fig. 4. (a) FT-IR spectra, (b) DTG curves, and (c) FWHW of Raman D band for GO-VC-*x* films. XPS C 1s spectra of (d) GO-VC-0%, (e) GO-VC-8%, and (f) GO-VC-20%. (A colour version of this figure can be viewed online.)

(instead of reducing GO) has decreased the C/O value for $x = 20\%$, since the C/O ratio in pure VC is 1. The following functional groups: C—C (284.8 eV), C—O (286.8 eV), C═O (288.2–288.4 eV), and C(O)O (289.0–289.4 eV) can be seen from C1s spectra [32], as shown in Fig. 4d–f and Table S3. As can be seen, the fraction of C—C and C═O peaks increases with the existence of VC, and that for C—O (C—OH) peak decreases, verifying the transformation of C—O into C—C by the pre-reduction of VC.

As shown in the Raman spectra in Fig. 5a, the D-band disappears and the G-band becomes narrower, indicating an efficient restoration of graphitic conjugation in rGO-VC-*x* films. The detailed Lorentzian fitting in Fig. 5b and c shows that, the G′ peaks of rGO-VC-0% and rGO-VC-8% are both composed of turbostratic stacked graphite (G'_{2D}) and AB Bernal stacked graphite (G'_{3DA}, G'_{3DB}). The relative fraction of turbostratic stacking is calculated to be 13.6% and 22.8%, for rGO-VC-0% and rGO-VC-8%, respectively, according to Cançado's equation [33]. Previous studies show that the turbostratic stacking may help to reduce the phonon scattering between layers due to the weak interlayer coupling [34], which may enhance the phonon transport in the plane [35]. From XRD patterns in Fig. 5c, the FWHM of (002) plane is obviously reduced in rGO-VC-5% and rGO-VC-8% films. The crystallite size (Lc) for rGO-VC-0%, rGO-VC-5% and rGO-VC-8% are estimated to be 53.9, 69.3 and 76.0 nm, using the Scherrer equation [36]. The FWHM of rGO-VC-*x* ($x = 5, 8$) films decreases obviously after the introduction of VC, indicating that the existence of VC has improved the crystallinity after annealing, although more VC caused wider FWHM in the XRD of GO-VC-*x* films. On the other hand, Fig. 5d shows that, although with more uniform distribution of interlayer distance, the interlayer spacing of rGO-VC-5% or rGO-VC-8% films is larger than that in bare GO, possibly due to the higher content of turbostratic stacking of VC involved films.

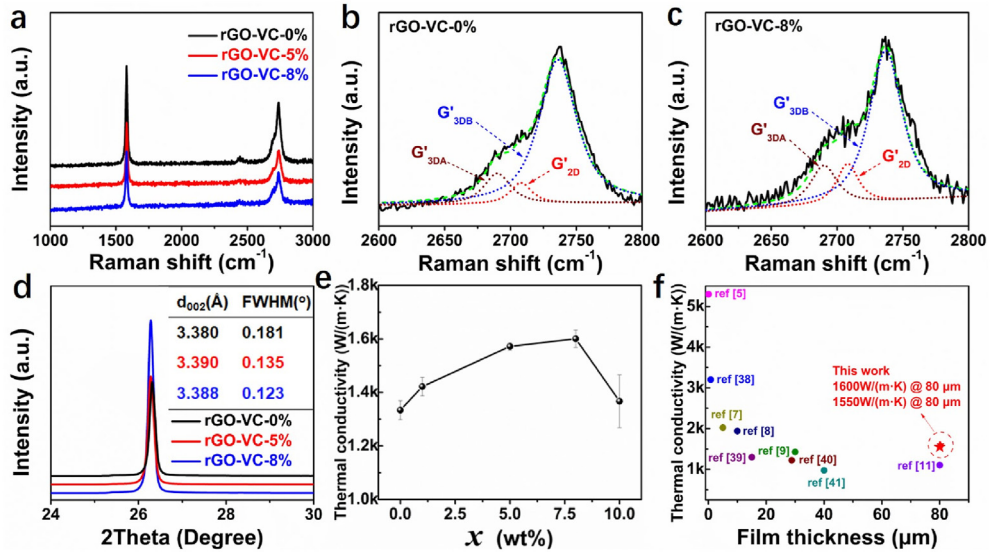

Fig. 5. (a) Raman spectra of rGO-VC-*x* films. Lorentzian fitting of Raman G′ peaks of (b) rGO-VC-0% film and (c) rGO-VC-8% film. (d) XRD pattern of rGO-VC-*x* films. (e) In-plane thermal conductivity of rGO-VC-*x* films. (f) Comparison of rGO-VC-*x* films with other reported values [38–41]. (A colour version of this figure can be viewed online.)

The in-plane thermal conductivity of rGO-VC-*x* films has been evaluated using a laser flash method and more details are included in the experimental session. As can be seen from Fig. 5e and Table S1, the thermal conductivity of rGO-VC-*x* films generally increases as the VC ratio increases till *x* of 8%, from which a thermal conductivity of 1603 W/(m·K) is demonstrated. When the VC ratio is further increased, *e.g.*, to 10%, the thermal conductivity decreases to the level of bare rGO films. From the comparison shown in Fig. 5f, the in-plane thermal conductivity of rGO-VC-8% is superior to previously reported films with the similar thickness [11]. The cross-plane thermal conductivity of rGO-VC-*x* films was also tested (Table S2), which is far lower than the in-plane values. An industrial scale preparation of rGO-VC-8% films has been demonstrated (Fig. S1), from which 200 m^2 rGO-VC-8% films show a thickness of 80 ± 5 μm and an averaged thermal conductivity of 1550 ± 50 W/(m·K), exceeding the performance of commercially available artificial graphite membranes in the market [37].

4. Conclusion

In summary, we have introduced VC to achieve moderate pre-reduction of GO before thermal annealing process to achieve a GF with high thermal conductivity and thickness. The reduction of GO by VC transformed some functional groups (*e.g.*, COOH, C═O) to those (*e.g.*, C—OH, C—O) which can decompose at a lower temperature, leading to less gas species in the annealing. Meanwhile, the introduction of VC improved the assembly orderings of the thermally annealed films, which contained a larger fraction of turbostratic stacking and larger interlayer distance. As a result, the GFs prepared through a blade coating process with VC mass ratio of 8% demonstrated a thermal conductivity of 1603 W/(m·K) with thickness of 80 μm, higher than the state-of-the-art graphitic thermal dispersion films.

Author statement

We thank everyone contributed to this paper. Zuo Pan and Yanhong Wu performed the material preparation and wrote the manuscript. Hong Yuan contributed to theoretical analyses and revised this manuscript. Runli Tang Lei Ji and Bucun Zhou helped to analyze thermal conductive data. Chuanren Ye helped to analyze structural characterizations. Dawei Zhang, Yan Qu, Hengxing Ji and Yanwu Zhu supervised the study and revised the manuscript. All authors have given approval to the final version of the manuscript.

Declaration of competing interest

The authors declare that they have no known competing financial interests or personal relationships that could have appeared to influence the work reported in this paper.

Acknowledgment

This work was supported by National Key R&D Program of China (Grant No. 2020YFA0711502), Natural Science Foundation of China (Nos. 51772282, 51972299).

Appendix A. Supplementary data

Supplementary data to this article can be found online at https://doi.org/10.1016/j.carbon.2021.06.058.

References

[1] M. Murakami, N. Nishiki, K. Nakamura, J. Ehara, H. Okada, T. Kouzaki, K. Watanabe, T. Hohshi, S. Yoshimur, High-quality and highly oriented graphite block from polycondensation polymer films, Carbon 30 (1992) 255–262.
[2] M. Inagaki, Y. Kaburagi, Y. Hishiyama, Thermal management material: graphite, Adv. Eng. Mater. 16 (2014) 494–506.
[3] H. Hatori, Y. Yamada, M. Shiraishi, In-plane orientation and graphitizability of polymide films:II. film thickness dependence, Carbon 31 (1993) 1307–1312.
[4] Y. Kaburagi, T. Kimura, A. Yoshida, Y. Hishiyama, Thermal and electrical conductivity and magnetoresistance of graphite films prepared from aromatic polyimide films, Tanso 253 (2012) 106–115.
[5] A.A. Balandin, S. Ghosh, W. Bao, I. Calizo, D. Teweldebrhan, F. Miao, C.N. Lau, Superior thermal conductivity of single layer graphene, Nano Lett. 8 (2008) 902–907.
[6] D.A. Dikin, S. Stankovich, E.J. Zimney, R.D. Piner, G.H.B. Dommett, G. Evmenenko, et al., Preparation and characterization of graphene oxide paper, Nature 448 (2007) 457–460.
[7] A. Akbari, B.V. Cunning, S.R. Joshi, C. Wang, D.C. Camacho-Mojica, S. Chatterjee, et al., Highly ordered and dense thermally conductive graphitic films from a graphene oxide/reduced graphene oxide mixture, Matter 2 (2020) 1–9.
[8] L. Peng, Z. Xu, Z. Liu, Y. Guo, P. Li, C. Gao, Ultrahigh thermal conductive yet superflexible graphene films, Adv. Mater. 29 (2017) 1700589.
[9] Y. Li, Y. Zhu, G. Jiang, Z.P. Cano, J. Yang, J. Wang, et al., Boosting the heat dissipation performance of graphene/polyimide flexible carbon film via enhanced through-plane conductivity of 3D hybridized structure, Small (2020) 1903315.
[10] J. Xi, Y. Li, E. Zhou, Y. Liu, W. Gao, Y. Guo, et al., Graphene aerogel films with expansion enhancement effect of high-performance electromagnetic interference shielding, Carbon 135 (2018) 44–51.
[11] F. Xu, R. Chen, Z. Lin, X. Sun, S. Wang, W. Yin, et al., Variable densification of reduced graphene oxide foam into multifunctional high-performance graphene paper, J. Mater. Chem. C 6 (2018) 12321–12328.
[12] H.C. Schniepp, Je-Luen Li, M.J. McAllister, H. Sai, M. Herrera-Alonso, D.H. Adamson, et al., Functionalized single graphene sheets derived from splitting graphite oxide, J. Phys. Chem. B 110 (2006) 8535–8539.
[13] S. Chen, Q. Wang, M. Zhang, R. Huang, Y. Huang, J. Tang, et al., Scalable production of thick graphene film for next generation thermal management application, Carbon 167 (2020) 270–277.
[14] J.D. Renteria, S. Ramirez, H. Malekpour, B. Alonso, A. Centeno, A. Zurutuza, et al., Strongly anisotropic thermal conductivity of free-standing reduced graphene oxide films annealed at high temperature, Adv. Funct. Mater. 25 (2015) 4664–4672.
[15] A.V. Krasheninnikov, F. Banhart, Engineering of nanostructured carbon materials with electron or ion beams, Nat. Mater. 6 (2007) 723–733.
[16] D.L. Nika, A.A. Balandin, Phonons and thermal transport in graphene and graphene-based materials, Rep. Prog. Phys. 80 (2017) 36502.
[17] A.A. Balandin, Phononics of graphene and related materials, ACS Nano 14 (2020) 5170–5178.
[18] C. Gong, M. Acik, R.M. Abolfath, Y. Chabal, K. Cho, Graphitization of graphene oxide with ethanol during thermal reduction, J. Phys. Chem. C 116 (2012) 9969–9979.
[19] C.B. Kim, J. Lee, J. Cho, M. Goh, Thermal conductivity enhancement of reduced Graphene oxide via chemical defect healing for efficient heat dissipation, Carbon 139 (2018) 386–392.
[20] H. Malekpour, K.-H. Chang, J.-C. Chen, C.-Y. Lu, D.L. Nika, K.S. Novoselov, A.A. Balandin, Thermal conductivity of graphene laminate, Nano Lett. 14 (2014) 5155–5161.
[21] J. Gao, F. Liu, Y. Liu, N. Ma, Z. Wang, X. Zhang, Environment-friendly method to produce graphene that employs vitamin C and amino acid, Chem. Mater. 22 (2010) 2213–2218.
[22] W.S. Hummers, R.E. Offeman, Preparation of graphitic oxide, J. Am. Chem. Soc. 80 (1958) 1339.
[23] M.J. Fernandez-Merino, L. Guardia, J.I. Paredes, S. Villar-Rodil, P. Solıs-Fernandez, A. Martınez-Alonso, J.M.D. Tascon, Vitamin C is an ideal substitute for hydrazine in the reduction of graphene oxide suspensions, J. Phys. Chem. C 114 (2010) 6426–6432.
[24] Z. Xu, C. Gao, Graphene chiral liquid crystals and macroscopic assembled fibres, Nat. Commun. 2 (2012) 571.
[25] T. Szabo, O. Berkesi, P. Forgo, K. Josepovits, Y. Sanakis, D. Petridis, I. Dekany, Evolution of surface functional groups in a series of progressively oxidized graphite oxides, Chem. Mater. 18 (2006) 2740–2749.
[26] Y. Shen, V. Boffa, I. Corazzari, A. Qiao, H. Tao, Y. Yue, Revealing hidden endotherm of Hummers' graphene oxide during low-temperature thermal reduction, Carbon 138 (2018) 337–347.
[27] M. Acik, G. Lee, C. Mattevi, A. Pirkle, R.M. Wallace, M. Chhowalla, et al., The role of oxygen during thermal reduction of graphene oxide studied by infrared absorption spectroscopy, J. Phys. Chem. C 115 (2011) 19761–19781.
[28] K.N. Kudin, B. Ozbas, H.C. Schniepp, R.K. Prud'homme, I.A. Aksay, R. Car, Raman spectra of graphite oxide and functionalized graphene sheets, Nano Lett. 8 (2008) 36–41.
[29] A. Kaniyoor, S. Ramaprabhu, A Raman spectroscopic investigation of graphite oxide derived graphene, AIP Adv. 2 (2012), 032183.
[30] A.C. Ferrari, J. Robertson, Interpretation of Raman spectra of disordered and amorphous carbon, Phys. Rev. B 61 (2000) 14095–14107.
[31] S. Eigler, C. Dotzer, A. Hirsch, Visualization of defect densities in reduced

graphene oxide, Carbon 50 (2012), 3666-2673.
[32] D.R. Dreyer, S. Park, C.W. Bielawski, R.S. Ruoff, The chemistry of graphene oxide, Chem. Soc. Rev. 39 (2010) 228–240.
[33] L.G. Cancado, K. Takai, T. Enoki, M. Endo, Y.A. Kim, H. Mizusaki, et al., Measuring the degree of stacking order in graphite by Raman spectroscopy, Carbon 46 (2008) 272–275.
[34] L.M. Malard, M.A. Pimenta, G. Dresselhaus, M.S. Dresselhaus, Raman spectroscopy in graphene, Phys. Rep. 473 (2009) 51–87.
[35] C.A. Klein, M.G. Holland, Thermal conductivity of pyrolytic graphite at low temperatures. I. turbostratic structures, Phys. Rev. 136 (1964) A575–A590.
[36] M.S. Seehra, A.S. Pavlovic, X-ray diffraction, thermal expansion, electrical conductivity, and optical microscopy studies of coal-based graphites, Carbon 31 (1993) 557–564.
[37] P. Huang, Y. Li, G. Yang, Z. Li, Y. Li, N. Hu, et al., Graphene film for thermal management: a review, Nano Mater. Sci. (2020), https://doi.org/10.1016/j.nanoms.2020.09.001.
[38] N. Wang, M.K. Samani, H. Li, L. Dong, Z. Zhang, P. Su, et al., Tailoring the thermal and mechanical properties of graphene film by structural engineering, Small (2018) 1801346.
[39] J. Li, X. Chen, R. Lei, J. Lai, T. Ma, Y. Li, Highly thermally conductive graphene film produced using glucose under low-temperature thermal annealing, J. Mater. Sci. 54 (2019) 7553–7562.
[40] T.-W. Pan, W.-S. Kuo, N.-H. Tai, Tailoring anisotropic thermal properties of reduced graphene oxide/multi-walled carbon nanotube hybrid composite films, Compos. Sci. Technol. 151 (2017) 44–51.
[41] Q.-Q. Kong, Z. Liu, J.-G. Gao, C.-M. Chen, Q. Zhang, G. Zhou, et al., Hierarchical graphene–carbon fiber composite paper as a flexible lateral heat spreader, Adv. Funct. Mater. 24 (2014) 4222–4228.